Scripta Materialia 204 (2021) 114132

Contents lists available at ScienceDirect

Scripta Materialia

journal homepage: www.elsevier.com/locate/scriptamat

# A novel bulk eutectic high-entropy alloy with outstanding as-cast specific yield strengths at elevated temperatures

Mingliang Wang[a], Yiping Lu[a,*], Tongmin Wang[a], Chuan Zhang[b], Zhiqiang Cao[a], Tingju Li[a], Peter K. Liaw[c]

[a] Key Laboratory of Solidification Control and Digital Preparation Technology (Liaoning Province), School of Materials Science and Engineering, Dalian University of Technology, Dalian, 116024, China
[b] CompuTherm LLC, Middleton, WI, 53562, United States
[c] Department of Materials Science and Engineering, The University of Tennessee, Knoxville, TN 37996, United States

ARTICLE INFO

*Article history:*
Received 25 May 2021
Revised 28 June 2021
Accepted 30 June 2021
Available online 13 July 2021

*Keywords:*
Eutectic high-entropy alloy
$L2_1$ structure
Hardness
Specific yield strength

ABSTRACT

Due to their excellent properties and great potential for industrial application, eutectic high-entropy alloys (EHEAs) have been a hot topic of study over the past few years. The current study reports a novel $AlCr_{1.3}TiNi_2$ EHEA with a low density and outstanding mechanical properties at elevated temperatures. A kilogram-scale EHEA ingot with uniform and ultrafine $L2_1$ and BCC lamellar structures (interlamellar spacing ~ 400 nm) was firstly prepared by a direct solidification method. The as-cast $AlCr_{1.3}TiNi_2$ EHEA exhibits much higher room- and high-temperature hardness and specific yield strength values than most reported refractory high-entropy alloys (RHEAs), EHEAs, and conventional Ni- and Ti-based alloys.



Developing lightweight, low-cost, and energy-efficient structural materials that exhibit excellent properties at elevated temperatures has been a pursuit of researchers. To date, the highest service temperature of traditional Ni-based superalloys, which are widely used in gas-turbine engines and aero engines, has reached 80% of their melting points [1]. Thus, these superalloys cannot meet the harsher service requirements that accompany further increases in the working temperature. In addition, Ni-based superalloys have inherently high densities and are expensive. Therefore, there is an urgent demand for the development of a new generation of lightweight, high-strength, and low-cost structural alloys for high-temperature applications.

Eutectic high-entropy alloys (EHEAs), which combine the advantages of high-entropy alloys (HEAs) [2,3] and eutectic alloys and exhibit a controllable, near-equilibrium microstructure that can resist changes in temperature up to the eutectic reaction point, are excellent candidates for high-temperature applications [4,5]. In particular, EHEAs present good castability and can be manufactured as industrial-scale ingots via direct casting, and the considerable compositional inhomogeneity typically observed in HEAs can be alleviated. Hence, good mechanical properties have also been obtained [6]. The first EHEA, $AlCoCrFeNi_{2.1}$, was developed by Lu et al. in 2014 [4]. Since then, this EHEA has received worldwide interest due to its combination of superior strength and ductility [7–13]. Meanwhile, dozens of new EHEA systems have been designed and investigated: $AlCrFeNiMo_{0.2}$ [14], $Co_2Mo_{0.8}Ni_2VW_{0.8}$ [15], $Nb_{25}Sc_{25}Ti_{25}Zr_{25}$ [16], $Co_{20}Cu_{20}Fe_{20}Ni_{20}Ti_{20}$ [17], $Zr_{0.6}CoCrFeNi_{2.0}$ [18], $Al_{1.3}CrFeNi$ [19], CoCrFeNiMnPd [20], $Fe_{20}Co_{20}Ni_{41}Al_{19}$ [21,22], $CoCrFeNiNb_{0.45}$ [23], $CoCrFeNiTa_x$ [24], $CoCrFeNiTa_{0.395}$ [25], $Al_{16}Co_{41}Cr_{15}Fe_{10}Ni_{18}$ [26], $Co_{30}Cr_{10}Fe_{10}Al_{18}Ni_{32-x}Mo_x$ [27], $CrFeNi_{(3-x)}Al_x$ [28], $Co_{25}Fe_{25}Mn_5Ni_{25}Ti_{20}$ [29], $Co_{25.1}Cr_{18.8}Fe_{23.3}Ni_{22.6}Ta_{8.5}Al_{1.7}$ [30], and so on. By compiling the eutectic phases observed in these reported EHEAs, it was found that they mainly consist of face-centered-cubic (FCC) and B2 phases or FCC and Laves phases. Among these phases, the FCC phase is known to be ductile, but it has a low strength. The B2 phase has a high room-temperature strength but poor creep resistance at elevated temperatures. The Laves phase exists as different polytypes, including the hexagonal C14, cubic C15, and hexagonal C36. However, the most stable polytype remains unclear. In particular, transformations in the Laves phase occur with changes in the temperature and/or applied stress [31,32], which makes it difficult to control its microstructure and properties in EHEAs. Additionally, the Laves phase exhibits severe room-temperature brittleness [33,34]. As such, the reported EHEA systems are not yet suitable for high-temperature applications.

Motivated by the above concerns, a lightweight and low-cost bulk $AlCr_{1.3}TiNi_2$ EHEA was developed. The as-cast $AlCr_{1.3}TiNi_2$

* Corresponding author.
*E-mail address:* luyiping@dlut.edu.cn (Y. Lu).

https://doi.org/10.1016/j.scriptamat.2021.114132
1359-6462/

EHEA exhibits much higher room- and high-temperature hardness and specific yield strength (SYS) values than most reported EHEAs, refractory HEAs (RHEAs), and conventional alloys, such as Inconel 718 and Ti-6Al-4 V.

A bulk alloy ingot with a nominal composition of $AlCr_{1.3}TiNi_2$ (atomic percent, at%) was prepared by electromagnetic levitation melting, using Al, Cr, Ti, and Ni raw materials with purities > 99.9 wt percent (wt%). Approximately 2.0 kg of master alloy was melted, superheated and poured into a graphite crucible with the length of 150 mm and inner diameter of 50 mm. The ingot was melted twice to ensure homogeneity. The density of the bulk ingot was measured by the Archimedes drainage method, using a ME204E balance with a precision of 0.0001 g. The thermal behavior of the as-cast alloy was analyzed, employing a Netzsch STA 449 F3 differential scanning calorimeter (DSC) from 50 to 1600 °C with a heating/cooling rate of 10 °C/min. in an argon atmosphere. The phase constituents of the alloy were identified by X-ray diffraction (XRD, Empyrean, Holland) with Cu $K_\alpha$ radiation between a scanning $2\theta$ range of 20 and 100° and at a scanning rate of 4° $min.^{-1}$.

Microstructural characterizations were performed, using scanning electron microscopy (SEM, NOVA NanoSEM 450), electron backscattered diffraction (EBSD, FEI Quanta 650F SEM equipped with the HKL Channel 5 software) and transmission electron microscopy (TEM, FEI Tecnai G2 F20 S-TWIN operating at 200 kV). Sharp tip specimens for three-dimensional (3D) atom probe tomography (3DAPT) were prepared with a dual-beam focused ion beam (FIB, FEI Helios Nanolab 600i). 3DAPT data were acquired, using a local electrode atom probe (LEAP 4000 × HR). The CAMECA integrated visualization and analysis software (IVAS 3.6.8) was used for data processing and 3D atomic reconstruction. The CALculated PHase Diagram (CALPHAD) method was used to predict phase formation trends of the $AlCr_{1.3}TiNi_2$ alloy. The Pandat 2016.1 software and its PanHEA2017 database, developed by CompuTHerm LLC, were used for thermodynamic calculations.

The hot hardness of the bulk samples was measured, employing a high-temperature Vickers hardness tester (HTV-PHS30, England). Uniaxial compression tests were conducted on as-cast samples of Φ8 mm × 12 mm at room temperature, 400, 600, 700, 800, 900, 1000, and 1100 °C, using a thermo-mechanical simulator (Gleeble3800) operating at a strain rate of $10^{-3}\ s^{-1}$.

Fig. 1a shows the macromorphology of the as-cast $AlCr_{1.3}TiNi_2$ ingot after slight surface polishing and reveals that the alloy exhibits excellent castability and no obvious shrinkage defects. The measured density of the bulk alloy is 6.43 $g/cm^3$, which is very close to its theoretical density of 6.47 $g/cm^3$ and further indicates that its microstructure is dense. As shown in Fig. 1b, the low-magnification SEM backscattered electron (BSE) image reveals that the as-cast alloy exhibits a uniform and ultrafine lamellar microstructure. The magnified BSE image in Fig. 1c indicates that the average interlamellar spacing is approximately 400 nm.

The XRD pattern presented in Fig. 1d reveals that the $AlCr_{1.3}TiNi_2$ alloy consists of BCC and $L2_1$ phases. The low-angle superlattice diffraction peaks at $2\theta$ values of 26.1° and 30.3° are attributed to the (111) and (200) planes of the ordered $L2_1$ phase, respectively, which has a calculated lattice parameter ($a_{L21}$) of 0.5895 nm. The lattice parameter of the BCC phase ($a_{BCC}$) was calculated to be 0.2892 nm. The lattice misfit ($\delta$) between the BCC and $L2_1$ phases can be calculated by $\delta = 2(a_{L21}-2a_{BCC})/(a_{L21}+2a_{BCC})$ [35,36], and the value of $\delta$ was determined to be 1.90%, which indicates that the interface between the two phases is semicoherent. The EBSD phase map shown in Fig. 1e further confirms the presence of both the BCC and $L2_1$ phases. The fine lamellae (with an average width of ~ 270 nm) have the BCC structure, while the coarse lamellae (with an average width of ~ 510 nm) have the $L2_1$ structure. The DSC results presented in Fig. 1f, including both heating and cooling curves, indicate the presence of only one melting event, which substantiates the eutectic composition in the $AlCr_{1.3}TiNi_2$ alloy.

A detailed TEM analysis was conducted to further identify the morphology and crystal structure of the eutectic phases (Fig. 2). Similar to the SEM and EBSD observations, the bright-field (BF) TEM image shown in Fig. 2a also reveals the typical dual-phase eutectic morphology. The selected area diffraction pattern (SADP) obtained for the fine lamellar phase along the [001] zone axis exhibits the reflections of a disordered BCC structure (Fig. 2b), while the SADP in Fig. 2c indicates that the coarse lamellar phase has an ordered $L2_1$ structure, which is in agreement with results of XRD and EBSD. The dark-field (DF) TEM image corresponding to the BF TEM image is shown in Fig. 2d and reveals a high density of nanoprecipitates within the $L2_1$ phase. The magnified DF TEM image in Fig. 2e further indicates that these nanoprecipitates tend to be distributed within the central region of the $L2_1$ phase. Evidently, there is a precipitate-free zone (PFZ) with a width of approximately 100 – 150 nm close to the BCC phase.

Fig. 2f shows a magnified BF TEM image corresponding to the central region of the $L2_1$ phase, which reveals that these nanoprecipitates are spherical with an average size of approximately 10 nm and are dispersed within the $L2_1$ matrix. Notably, a strain contrast can be clearly seen at the interface of the nanoprecipitate/$L2_1$ matrix, which suggests that these nanoprecipitates may be coherent with the $L2_1$ matrix. This is confirmed by the high-resolution TEM (HRTEM) image shown in Fig. 2g, wherein a representative spherical nanoprecipitate is embedded within the $L2_1$ matrix. A magnified HRTEM image showing the interface between the nanoprecipitate and $L2_1$ matrix is presented in the upper right inset of Fig. 2g and reveals that the atomic planes across the nanoprecipitate/$L2_1$ matrix interface are continuous. This further substantiates that the nanoprecipitate/$L2_1$ matrix interface is coherent. Electron-diffraction patterns of the nanoprecipitate and the $L2_1$ matrix along the [001] zone axis obtained from fast Fourier transform (FFT) are shown in the upper left inset and the lower right inset of Fig. 2g, respectively; the two electron-diffraction patterns indicate that the nanoprecipitate has a disordered BCC structure, while the matrix with an obvious $L2_1$ superlattice structure is ordered.

Additionally, the DF TEM image in Fig. 2e indicates that there are abundant dislocation networks along the interfaces between the BCC and $L2_1$ phases. A magnified HRTEM image from an inverse FFT (IFFT) corresponding to the interfacial region in Fig. 2e is presented in Fig. 2h. A high density of edge dislocations can be clearly observed. This feature indicates that the formation of interfacial dislocation networks is due to the lattice mismatch between the BCC and $L2_1$ phases, and the semicoherent BCC/$L2_1$ interface is further confirmed. Note that the formation of interfacial dislocation networks can relieve long-range internal stresses caused by the lattice mismatch [37]. The scanning TEM (STEM)-energy dispersive spectroscopy (EDS) maps in Fig. 2i reveal that the BCC-structured lamellar phase is Cr-rich, while the $L2_1$-structured lamellar phase is enriched with Al, Ti and Ni.

The 3DAPT was used to determine the exact compositions of the eutectic phases and nanoprecipitates (Fig. 3). The 3D-reconstruction ion maps of various elements presented in Fig. 3a show the interfacial region between the BCC and $L2_1$ phases. Evidently, the side of the $L2_1$ phase corresponds to the PFZ (see Fig. 2e). One-dimensional compositional profiles across the BCC/$L2_1$ interface (Fig. 3b) reveal that the BCC phase has an average composition of 92.55 at% Cr, 4.09 at% Ti, 2.63 at% Al, and 0.73 at% Ni, while the PFZ of the $L2_1$ phase has an average composition of 0.81 at% Cr, 25.32 at.% Ti, 24.54 at% Al and 49.33 at% Ni. Thus, the BCC phase, which contains more than 90 at% Cr, is Cr rich. The stoichiometry of the $L2_1$ phase that is rich in Ni, Al, and Ti can be

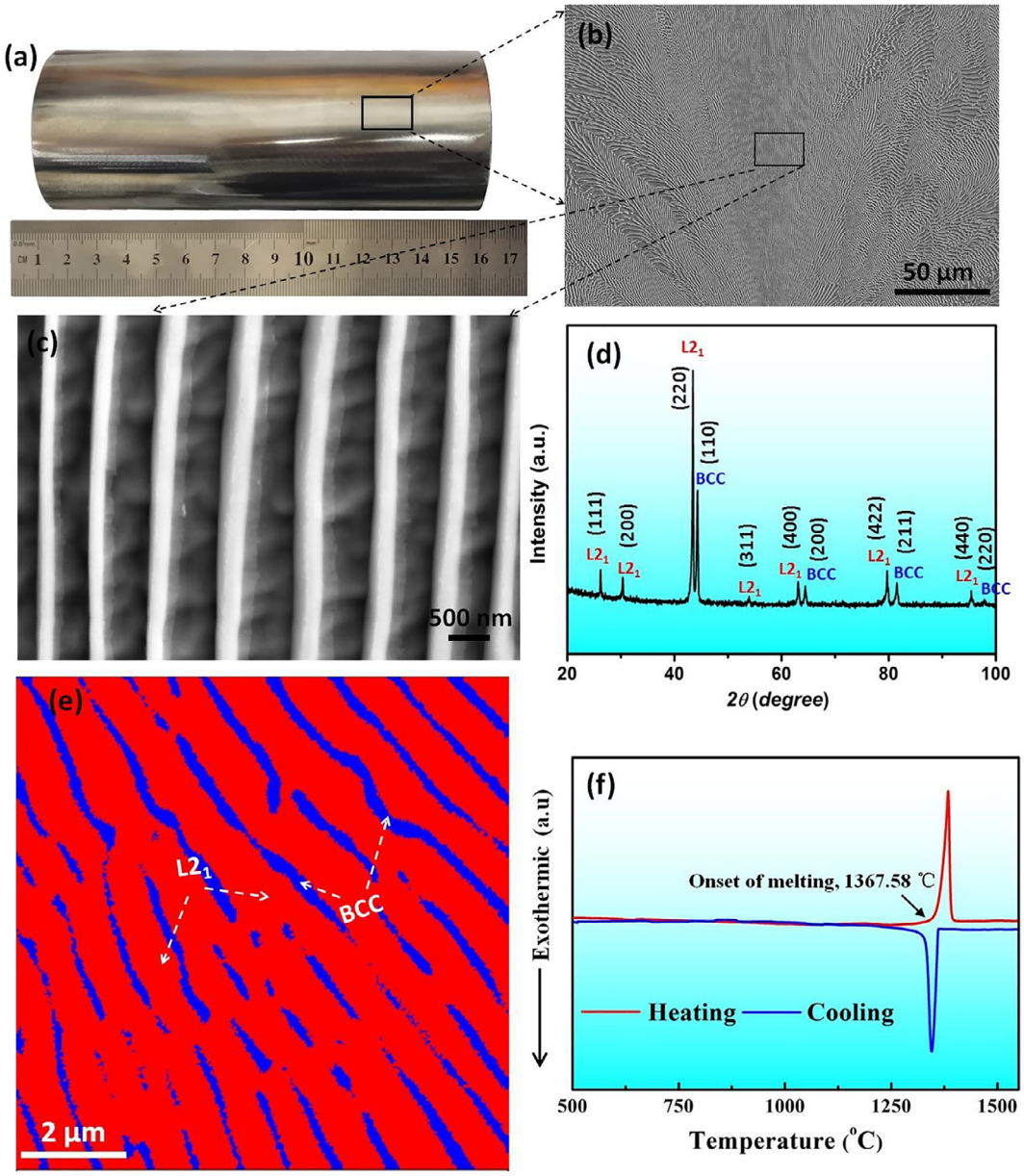


**Fig. 1.** (a) Macro-profile of the as-cast $AlCr_{1.3}TiNi_2$ alloy ingot. (b) SEM-BSE image of the $AlCr_{1.3}TiNi_2$ ingot. (c) The magnified SEM-BSE image of the $AlCr_{1.3}TiNi_2$ ingot. (d) XRD pattern of the $AlCr_{1.3}TiNi_2$ ingot. (e) EBSD phase map of the $AlCr_{1.3}TiNi_2$ ingot. (f) DSC curves of the as-cast $AlCr_{1.3}TiNi_2$ ingot.

described as $Ni_2AlTi$, which is a Heusler-like ordered phase with an $L2_1$ structure.

Fig. 3c shows 3D reconstruction ion maps of the various elements in the central region of the $L2_1$ phase. A high density of Cr-rich nanoprecipitates is observed within the $L2_1$ matrix, which is consistent with the results of TEM. The 3D reconstruction ion maps of the various elements corresponding to a typical nanoprecipitate are shown in Fig. 3d and clearly reveal the presence of Cr-atomic clusters. One-dimensional compositional profiles spanning the nanoprecipitate/$L2_1$ matrix interface (Fig. 3e) further indicate that Cr is partitioned into the nanoprecipitate. The composition of the nanoprecipitates was determined by extracting spheres of a 3-nm diameter from several nanoprecipitates to generate the bulk composition of these spheres. The results indicate that the nanoprecipitates have an average composition of 28.11 at% Cr, 18.27 at% Ti, 20.17 at% Al, and 33.45 at% Ni. The formation of the PFZ is mainly attributed to solute depletion because both the BCC lamellar phase and the nanoprecipitates are Cr rich, and the BCC lamellar phase forms prior to the nanoprecipitates. Hence, the growth of the BCC lamellar phase leads to the depletion of Cr in nearby regions [38,39]. In addition, the $Ni_2AlTi$ ($L2_1$)-Cr (BCC) pseudo-binary phase diagram was calculated, as shown in Fig. S1 (see Supporting information), from which both the eutectic reaction and the trend of precipitation of second phases can be predicted, which is consistent with the experimental observations.

The hardness values of the as-cast $AlCr_{1.3}TiNi_2$ EHEA from room temperature to 900 °C are summarized in Fig. 4a and compared with those of a typical EHEA ($AlCoCrFeNi_{2.1}$) [40], HEA ($Co_{1.5}CrFeNi_{1.5}Ti_{0.5}$) [41], and superalloy (Inconel 718) [41]. The hardness values of the $AlCr_{1.3}TiNi_2$ EHEA are much higher than those of $AlCoCrFeNi_{2.1}$ and Inconel 718 at both room and elevated temperatures. At room temperature, $AlCr_{1.3}TiNi_2$ and $Co_{1.5}CrFeNi_{1.5}Ti_{0.5}$ have similar hardness values, but the $AlCr_{1.3}TiNi_2$ EHEA far outperforms the $Co_{1.5}CrFeNi_{1.5}Ti_{0.5}$ HEA at higher temperatures. This trend indicates that the $AlCr_{1.3}TiNi_2$ EHEA has an outstanding high-temperature softening resistance

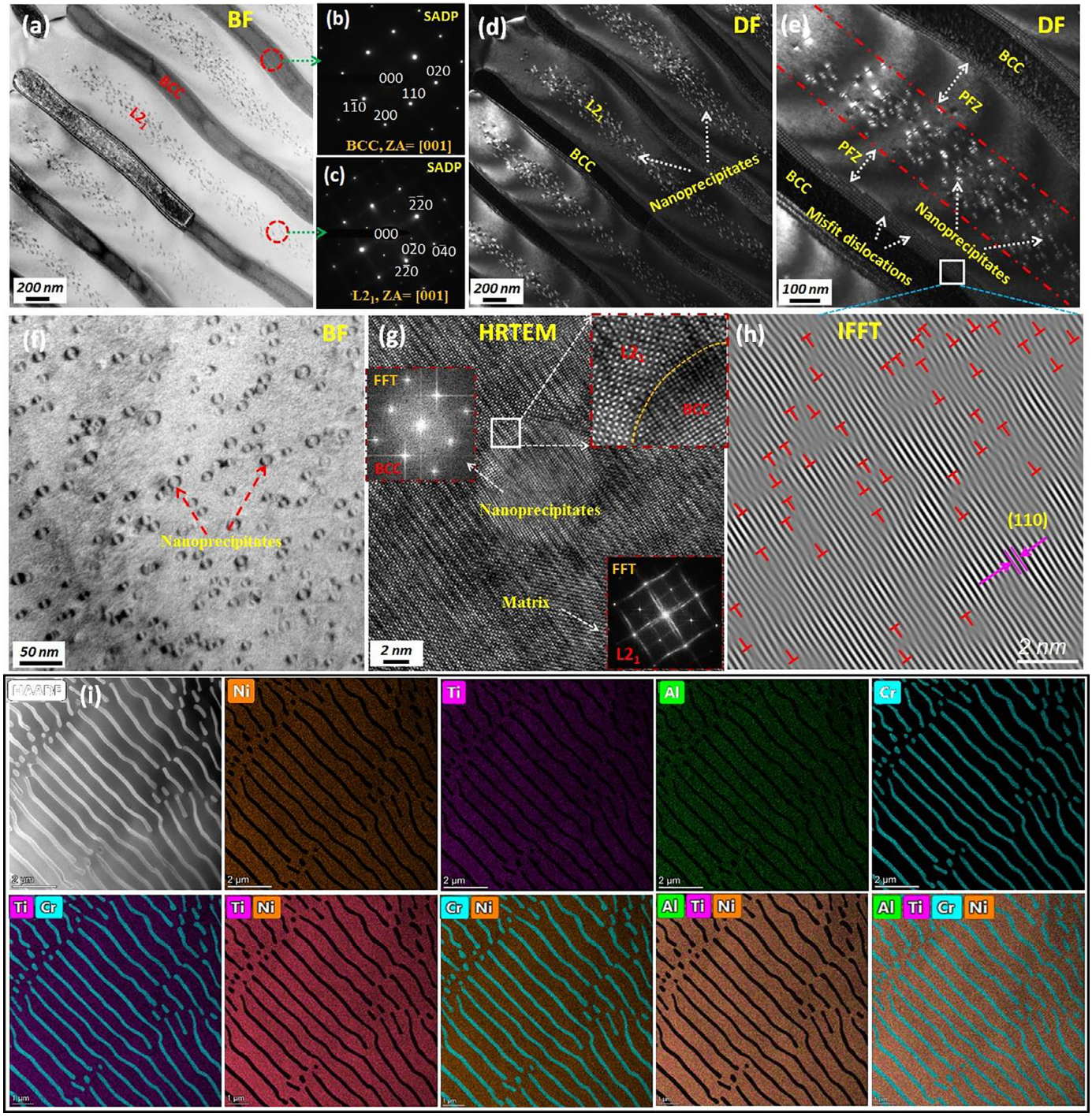


**Fig. 2.** TEM characterization of the $AlCr_{1.3}TiNi_2$ EHEA. (a) BF TEM image. (b) SADP of the fine lamellar phase. (c) SADP of the coarse lamellar phase. (d) DF TEM image. (e) The magnified DF TEM image. (f) A magnified BF TEM image corresponding to the central region of the $L2_1$ phase. (g) HRTEM image showing a nanoprecipitate embedded inside the $L2_1$ matrix. The upper right inset shows a magnified HRTEM image for the interface of the nanoprecipitate/$L2_1$ matrix; the upper left inset shows the electron-diffraction pattern of the nanoprecipitate from fast Fourier transform (FFT); the lower right inset shows the electron-diffraction pattern of the $L2_1$ matrix from FFT. (h) A magnified HRTEM image from inverse FFT (IFFT) showing the interfacial region in (e). (i) STEM-EDS elemental distribution maps.

with an average hardness value of 490.7 HV at 800 °C and 483.5 HV at 900 °C. These values are much higher than those of the $Co_{1.5}CrFeNi_{1.5}Ti_{0.5}$ HEA (~ 385 HV and ~ 346 HV) at the same temperatures. For long-term structural applications carried out at elevated temperatures, thermal stability is one of the most critical material requirements. The comparison of hot-hardness values presented in Fig. 4a indicates that the present EHEA is thermally stable at elevated temperatures.

Compression tests were conducted on the as-cast $AlCr_{1.3}TiNi_2$ EHEA from room temperature to 1100 °C at a strain rate of $1 \times 10^{-3}\ s^{-1}$, and the stress-strain curves are shown in Fig. 4b. The yield strength gradually decreases as the temperature increases, while the fracture strain gradually increases with increasing temperature. The samples did not fracture under a compressive strain above 50% at temperatures exceeding 800 °C, which suggests that the EHEA has an excellent high-temperature plasticity. Addi-

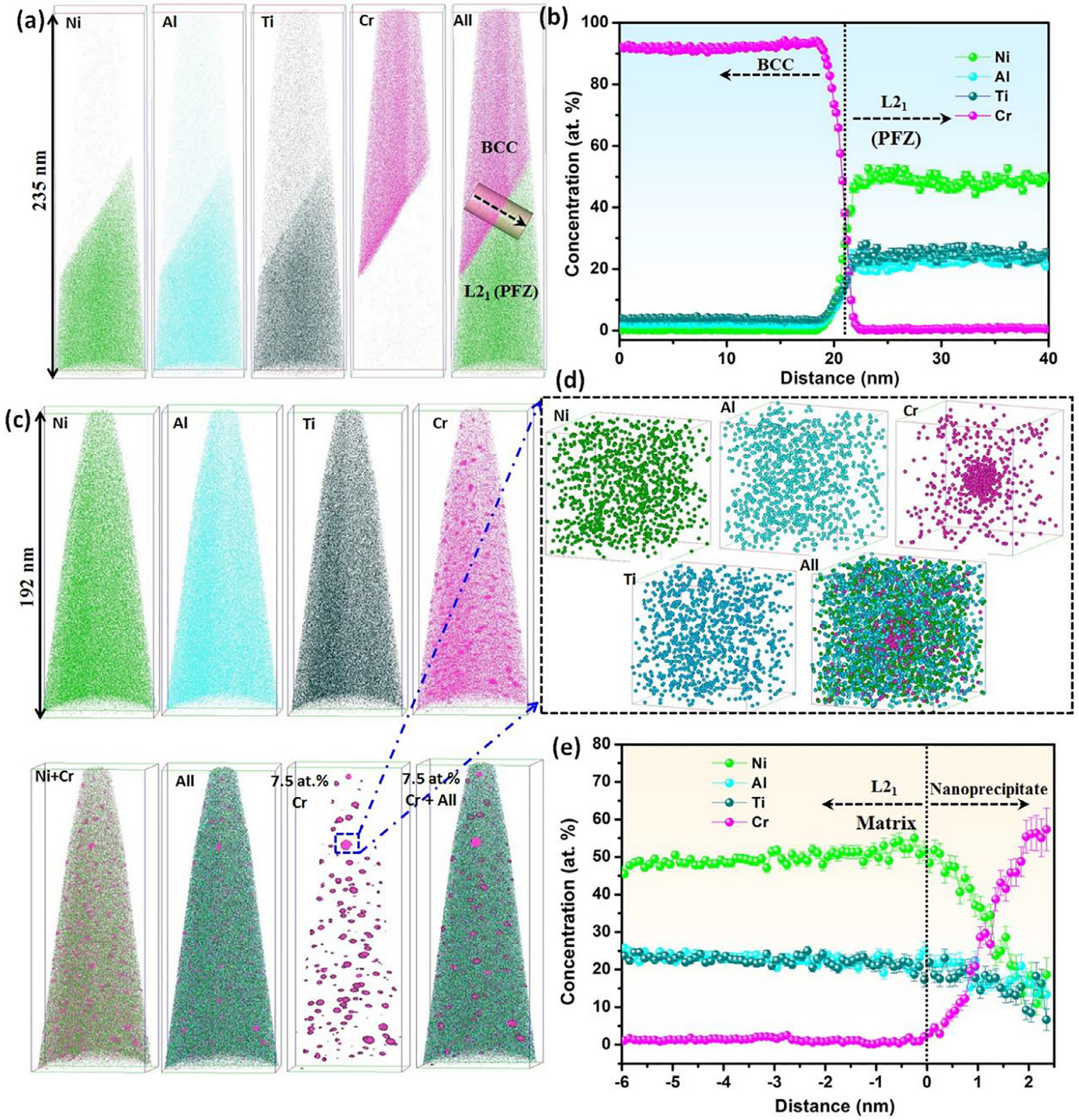


**Fig. 3.** APT characterization of the $AlCr_{1.3}TiNi_2$ EHEA. (a) 3D reconstruction of ion maps for various elements showing the interfacial region of BCC/$L2_1$. (b) One-dimensional compositional profiles across the interface of BCC/$L2_1$. (c) 3D reconstruction of ion maps for various elements corresponding to the central region of the $L2_1$ phase. (d) The 3D reconstruction of ion maps captured from a nanoprecipitate in (c). (e) One-dimensional compositional profiles across the interface of the nanoprecipitate/$L2_1$ matrix.

tionally, the stress-strain curves indicate that strain-hardening capability of the EHEA can be retained up to 800 °C.

Fig. 4c shows the temperature dependence of the SYS of the as-cast $AlCr_{1.3}TiNi_2$ EHEA and compares the results to those of reported RHEAs [42–47], HEAs [48], EHEAs [23], and conventional alloys, such as Ni-based superalloys [42], Ti-based alloys [49], and Al-based alloys [43]. The $AlCr_{1.3}TiNi_2$ EHEA exhibits the highest SYS at room temperature, with a value nearly identical to that of the $Al_2CoCrCuFeNi$ HEA. At temperatures between 400 and 600 °C, the $AlCr_{1.3}TiNi_2$ EHEA presents no apparent softening, and this EHEA has the highest SYS among the investigated alloys at 600 °C. The SYS of the $AlCr_{1.3}TiNi_2$ EHEA exhibits a decline when the temperature is above 600 °C. However, it still maintains a higher level. For instance, the SYS of the $AlCr_{1.3}TiNi_2$ EHEA is greater than that of the other alloys (with the exception of the AlNbTiV RHEA) at 800 °C. At 900 °C, the SYS of the $AlCr_{1.3}TiNi_2$ EHEA is only slightly lower than that of the NbTaTiV RHEA but much higher than those of the other alloys. In particular, the present EHEA exhibits

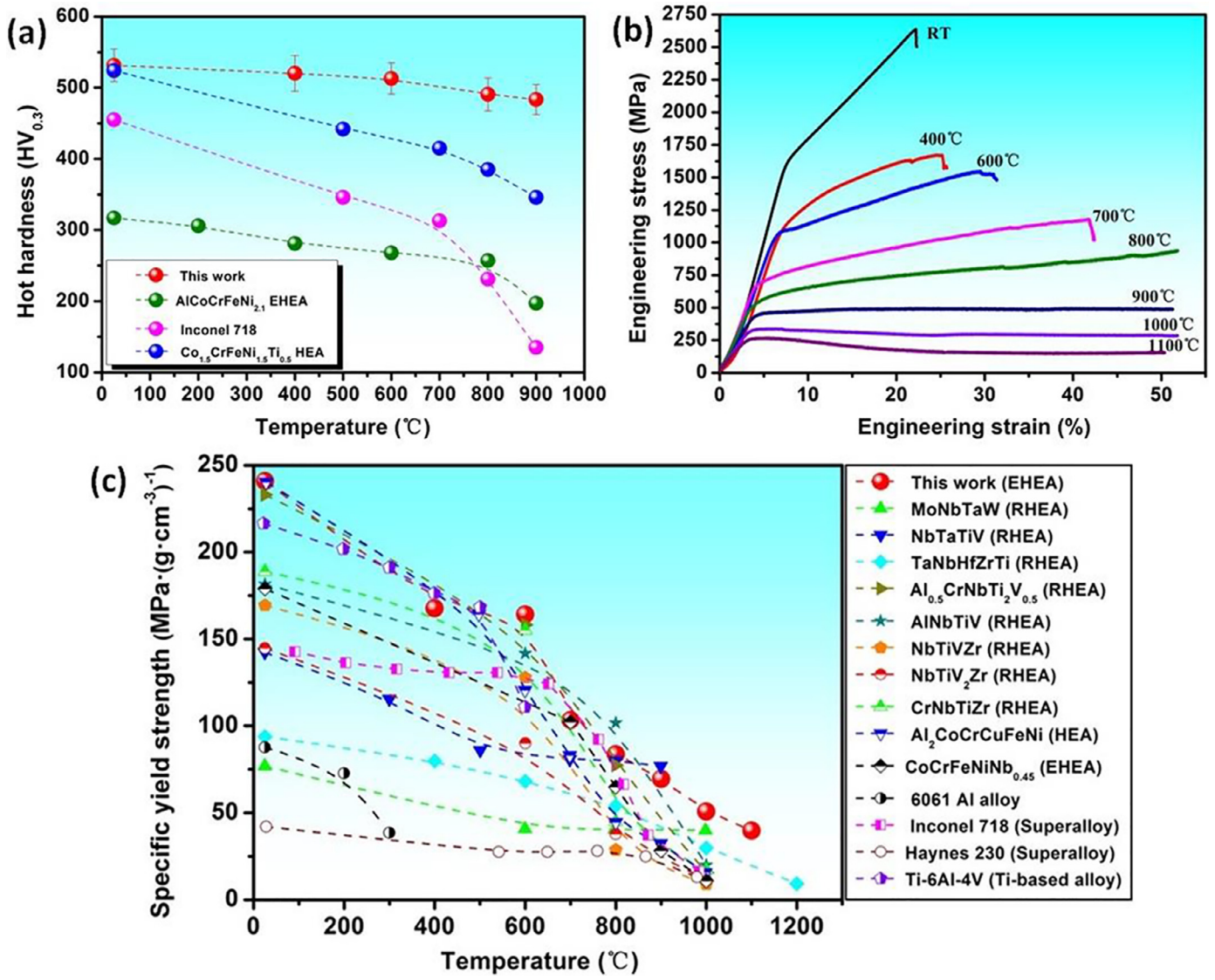


**Fig. 4.** (a) Comparison of the temperature dependence of hardness. (b) Compressive engineering stress-strain curves of the $AlCr_{1.3}TiNi_2$ EHEA at various temperatures. (c) Comparison of the temperature dependence of specific yield strength (SYS).

the highest SYS among the investigated alloys at both 1000 and 1100 °C, which indicates an excellent softening resistance at higher temperatures. In general, the SYSs of the conventional alloys, such as Ti-6Al-4 V and Inconel 718, are substantially reduced at certain temperatures (500 °C and approximately 650 °C, respectively), and their SYSs exhibit very low levels at higher temperatures. The SYSs of some RHEAs, such as NbTaTiV and MoNbTaW, do not substantially change as a function of temperature, but these values are low both at room temperature and high temperatures due to the high density of these materials. However, the $AlCr_{1.3}TiNi_2$ EHEA maintained the high SYS values both at room temperature and at high temperatures, which is attributed to the following aspects. First, the $AlCr_{1.3}TiNi_2$ EHEA contains a large amount of low-density elements, such as Al and Ti, which leads to the EHEA having a low density. Second, the near-equilibrium eutectic structures, which form an in-situ composite, can resist changes at temperatures as high as their eutectic reaction point. Third, the Ni-Al-Ti-rich $L2_1$ phase, which possesses an extremely stable Heusler-type structure with a high degree of order and limited slip systems, demonstrates an outstanding creep resistance [50,51]. Fourth, the eutectic phase interface of BCC/$L2_1$ is semi-coherent, which belongs to the strong interfacial combination with a high interfacial bonding strength [52,53]. Furthermore, both the large number of eutectic-phase interfaces and the high density of interfacial dislocations can hinder dislocation motion. Fifth, the high density of coherent nanoprecipitates within the $L2_1$ matrix can enhance the strength of the EHEA via precipitation strengthening.

In summary, a novel lightweight EHEA composed of the $L2_1$ and BCC phases was developed. The Heusler-like $L2_1$ phase was firstly found in EHEAs. A kilogram-scale $AlCr_{1.3}TiNi_2$ EHEA ingot with a uniform, ultrafine lamellar structure (interlamellar spacing ~ 400 nm) was successfully fabricated by a direct solidification method. The as-cast bulk EHEA exhibited much higher room- and high-temperature hardness and SYS values than most reported RHEAs, HEAs, EHEAs, and conventional alloys. In addition, the present EHEA also exhibited an outstanding softening resistance at higher temperatures. The current $AlCr_{1.3}TiNi_2$ EHEA is a very promising candidate for high-temperature service.

## Declaration of Competing Interest

The authors declare that they have no known competing financial interests or personal relationships that could have appeared to influence the work reported in this paper.

## Acknowledgments

This work was supported by the National Natural Science Foundation of China (Nos. 52001051, 51822402 and U20A20278), Liao Ning Revitalization Talents Program (No. XLYC1807047), Fund of the State Key Laboratory of Solidification Processing in NWPU (No. SKLSP201902), and the Project funded by China Postdoctoral Science Foundation (Nos. 2020M670747 and 2021T140082). P. K. Liaw appreciates support from the National Science Foundation (DMR-1611180 and 1809640) and the US Army Research Office (W911NF-13–1–0438 and W911NF-19–2–0049).

## Supplementary materials

Supplementary material associated with this article can be found, in the online version, at doi:10.1016/j.scriptamat.2021.114132.

## References

[1] R.C. Reed, The Superalloys: Fundamentals and Applications, Cambridge University Press, 2008.
[2] J.W. Yeh, S.K. Chen, S.J. Lin, J.Y. Gan, T.S. Chin, T.T. Shun, C.H. Tsau, S.Y. Chang, Adv. Eng. Mater. 6 (5) (2004) 299–303.
[3] Y. Zhang, T.T. Zuo, Z. Tang, M.C. Gao, K.A. Dahmen, P.K. Liaw, Z.P. Lu, Prog. Mater. Sci. 61 (2014) 1–93.
[4] Y.P. Lu, Y. Dong, S. Guo, L. Jiang, H.J. Kang, T.M. Wang, B. Wen, Z.J. Wang, J.C. Jie, Z.Q. Cao, H.H. Ruan, T.J. Li, Sci. Rep. 4 (2014) 6200.
[5] Y.P. Lu, Y. Dong, H. Jiang, Z.J. Wang, Z.Q. Cao, S. Guo, T.M. Wang, T.J. Li, P.K. Liaw, Scr. Mater. 187 (2020) 202–209.
[6] Y.P. Lu, X.Z. Gao, L. Jiang, Z.N. Chen, T.M. Wang, J.C. Jie, H.J. Kang, Y.B. Zhang, S. Guo, H.H. Ruan, Y.H. Zhao, Z.Q. Cao, T.J. Li, Acta Mater. 124 (2017) 143–150.
[7] I.S. Wani, T. Bhattacharjee, S. Sheikh, Y.P. Lu, S. Chatterjee, P.P. Bhattacharjee, S. Guo, N. Tsuji, Mater. Res. Lett. 4 (2016) 174–179.
[8] S. Shukla, T. Wang, S. Cotton, R.S. Mishra, Scr. Mater. 156 (2018) 105–109.
[9] T. Bhattacharjee, R. Zheng, Y. Chong, S. Sheikh, S. Guo, I.T. Clark, T. Okawa, I.S. Wani, P.P. Bhattacharjee, A. Shibata, N. Tsuji, Mater. Chem. Phys. 210 (2018) 207–212.
[10] T. Bhattacharjee, I.S. Wani, S. Sheikh, I.T. Clark, T. Okawa, S. Guo, P.P. Bhattacharjee, N. Tsuji, Sci. Rep. 8 (2018) 3276.
[11] P. Shi, W. Ren, T. Zheng, Z. Ren, X. Hou, J. Peng, P. Hu, Y. Gao, Y. Zhong, P.K. Liaw, Nat. Commun. 10 (2019) 489.
[12] H. Zheng, R. Chen, G. Qin, X. Li, Y. Su, H. Ding, J. Guo, H. Fu, Intermetallics 113 (2019) 106569.
[13] T. Xiong, S. Zheng, J. Pang, X. Ma, Scr. Mater. 186 (2020) 336–340.
[14] Y. Dong, L. Jiang, H. Jiang, Y. Lu, T. Wang, T. Li, Mater. Des. 82 (2015) 91–97.
[15] H. Jiang, H. Zhang, T. Huang, Y. Lu, T. Wang, T. Li, Mater. Des. 109 (2016) 539–546.
[16] Ł. Rogal, J. Morgiel, Z. Świątek, F. Czerwiński, Mater. Sci. Eng. A 651 (2016) 590–597.
[17] S. Samal, M.R. Rahul, R.S. Kottada, G. Phanikumar, Mater. Sci. Eng. A 664 (2016) 227–235.
[18] Y. Lu, H. Jiang, S. Guo, T. Wang, Z. Cao, T. Li, Intermetallics 91 (2017) 124–128.
[19] X. Chen, Y. Sui, J. Qi, Y. He, F. Wei, Q. Meng, Z. Sun, J. Mater. Res. 32 (2017) 2109–2116.
[20] Y. Tan, J. Li, J. Wang, H. Kou, Intermetallics 85 (2017) 74–79.
[21] X. Jin, Y. Zhou, L. Zhang, X. Du, B. Li, Mater. Lett. 216 (2018) 144–146.
[22] P. Shi, Y. Zhong, Y. Li, W. Ren, T. Zheng, Z. Shen, B. Yang, J. Peng, P. Hu, Y. Zhang, P.K. Liaw, Y. Zhu, Mater. Today 41 (2020) 62–71.
[23] H. Jiang, D. Qiao, Y. Lu, Z. Ren, Z. Cao, T. Wang, T. Li, Scr. Mater. 165 (2019) 145–149.
[24] C. Ai, F. He, M. Guo, J. Zhou, Z. Wang, Z. Yuan, Y. Guo, Y. Liu, L. Liu, J. Alloy. Compd. 735 (2018) 2653–2662.
[25] W. Huo, H. Zhou, F. Fang, X. Zhou, Z. Xie, J. Jiang, J. Alloy. Compd. 735 (2018) 897–904.
[26] A. Shafei, S. Rajabi, Appl. Phys. A 125 (2019) 783.
[27] Z. Yang, W. Z., Q. Wu, T. Zheng, P. Zhao, J. Zhao, J. Chen, Appl. Phys. A 125 (2019) 208.
[28] X. Jin, J. Bi, L. Zhang, Y. Zhou, X. Du, Y. Liang, B. Li, J. Alloy. Compd. 770 (2019) 655–661.
[29] R. Jain, M.R. Rahul, S. Samal, V. Kumar, G. Phanikumar, J. Alloy. Compd. 822 (2020) 153609.
[30] L. Han, X. Xu, Z. Li, B. Liu, C.T. Liu, Y. Liu, Mater. Res. Lett. 8 (10) (2020) 373–382.
[31] F. Stein, M. Palm, G. Sauthoff, Intermetallics 13 (2005) 1056–1074.
[32] M. Palm, G. Sauthoff, Intermetallics 12 (2004) 1345–1359.
[33] M. Wang, H. Cui, N. Wei, L. Ding, X. Zhang, Y. Zhao, C. Wang, Q. Song, ACS Appl. Mater. Interfaces 10 (2018) 4250–4265.
[34] Y. Zhao, M. Wang, H. Cui, Y. Zhao, X. Song, Y. Zeng, X. Gao, F. Lu, C. Wang, Q. Song, J. Alloy. Compd. 805 (2019) 585–596.
[35] R. Feng, M.C. Gao, C. Zhang, W. Guo, J.D. Poplawsky, F. Zhang, J.A. Hawk, J.C. Neuefeind, Y. Ren, P.K. Liaw, Acta Mater. 146 (2018) 280–293.
[36] Y. Ma, Q. Wang, B.B. Jiang, C.L. Li, J.M. Hao, X.N. Li, C. Dong, T.G. Nieh, Acta Mater. 147 (2018) 213–225.
[37] L.Y. Sheng, J.T. Guo, H.Q. Ye, Mater. Des. 96 (2009) 964–969.
[38] M.H. Tsai, Y. Yuan, G. Cheng, W. Xu, K.Y. Tsai, C.W. Tsai, W.W. Jian, C.C. Juan, W.J. Shen, M.H. Chuang, J.W. Yeh, Y.T. Zhu, Intermetallics 32 (2013) 329–336.
[39] M. Wang, H. Cui, Y. Zhao, C. Wang, N. Wei, Y. Zhao, X. Zhang, Q. Song, Mater. Des. 180 (2019) 107893.
[40] J. Miao, H. Liang, A. Zhang, J. He, J. Meng, Y. Lu, Tribol. Int. 153 (2021) 106599.
[41] Y.J. Chang, A.C. Yeh, J. Alloy. Compd. 653 (2015) 379–385.
[42] O.N. Senkov, G.B. Wilks, J.M. Scott, D.B. Miracle, Intermetallics 19 (5) (2011) 698–706.
[43] C. Lee, G. Song, M.C. Gao, R. Feng, P. Chen, J. Brechtl, Y. Chen, K. An, W. Guo, J.D. Poplawsky, S. Li, A.T. Samaei, W. Chen, A. Hu, H. Choo, P.K. Liaw, Acta Mater. 160 (2018) 158–172.
[44] O.N. Senkov, J.M. Scott, S.V. Senkova, F. Meisenkothen, D.B. Miracle, C.F. Woodward, J. Mater. Sci. 47 (2012) 4062–4074.
[45] N.D. Stepanov, N.Y. Yurchenko, E.S. Panina, M.A. Tikhonovsky, S.V. Zherebtsov, Mater. Lett. 188 (2017) 162–164.
[46] N.D. Stepanov, N.Y. Yurchenko, D.V. Skibin, M.A. Tikhonovsky, G.A. Salishchev, J. Alloy. Compd. 652 (2015) 266–280.
[47] O.N. Senkov, S.V. Senkova, D.B. Miracle, C. Woodward, Mater. Sci. Eng. A 565 (2013) 51–62.
[48] C.J. Tong, M.R. Chen, J.W. Yeh, S.J. Lin, S.K. Chen, T.T. Shun, S.Y. Chang, Metall. Mater. Trans. A 36 (5) (2005) 1263–1271.
[49] S. Zherebtsov, G. Salishchev, R. Galeyev, K. Maekawa, Mater. Trans. 46 (9) (2005) 2020–2025.
[50] P. Strutt, R. Polvani, J. Ingram, Metall. Mater. Trans. A 7 (1976) 23–31.
[51] W. Everhart, J. Newkirk, Heliyon 5 (2019) e01578.
[52] H.E. Cline, J.L. Walter, Metall. Trans. 1 (1970) 2907–2917.
[53] Z. Shang, J. Shen, L. Wang, Y. Du, Y. Xiong, H. Fu, Mater. Charact. 109 (2015) 152–159.